LAWRENCE
LIVERMORE
NATIONAL
LABORATORY

LLNL-PROC-662418

Controlling H-Mode Particle Transport with Modulated Electron Heating in DIII-D and Alcator C-Mod via TEM Turbulence

D. R. Ernst, K. H. Burrell, W. Guttenfelder, T. L. Rhodes, L. Schmitz, A. M. Dimits, E. J. Doyle, B. A. Grierson, M. Greenwald, C. Holland, G. R. McKee, R. Perkins, C. C. Petty, J. C. Rost, D. Truong, G. Wang, L. Zheng

October 10, 2014

25th IAEA Fusion Energy Conference
St. Petersburg, Russia
October 13, 2014 through October 18, 2014

Disclaimer

This document was prepared as an account of work sponsored by an agency of the United States government. Neither the United States government nor Lawrence Livermore National Security, LLC, nor any of their employees makes any warranty, expressed or implied, or assumes any legal liability or responsibility for the accuracy, completeness, or usefulness of any information, apparatus, product, or process disclosed, or represents that its use would not infringe privately owned rights. Reference herein to any specific commercial product, process, or service by trade name, trademark, manufacturer, or otherwise does not necessarily constitute or imply its endorsement, recommendation, or favoring by the United States government or Lawrence Livermore National Security, LLC. The views and opinions of authors expressed herein do not necessarily state or reflect those of the United States government or Lawrence Livermore National Security, LLC, and shall not be used for advertising or product endorsement purposes.

LLNL-PROC-662418

Controlling H-Mode Particle Transport with Modulated Electron Heating in DIII-D and Alcator C-Mod via TEM Turbulence

D.R. Ernst[1], K.H. Burrell[2], W. Guttenfelder[3], T.L. Rhodes[4], L. Schmitz[4], A.M. Dimits[5], E.J. Doyle[4], B.A. Grierson[3], M. Greenwald[1], C. Holland[6], G.R. McKee[7], R. Perkins[3], C.C. Petty[2], J.C. Rost[1], D. Truong[7], G. Wang[4], L. Zeng[4] and the DIII-D and Alcator C-Mod Teams

[1]MIT Plasma Science and Fusion Center, Cambridge, MA 02139, USA
[2]General Atomics, PO Box 85608, San Diego, CA 92186, USA
[3]Princeton Plasma Physics Laboratory, PO Box 451, Princeton, NJ 08543, USA
[4]University of California Los Angeles, PO Box 957099, Los Angeles, CA 90095, USA
[5]Lawrence Livermore National Laboratory, P.O. Box 808, Livermore, CA 94551, USA
[6]University of California San Diego, 9500 Gilman Dr., La Jolla, California 92093, USA
[7]University of Wisconsin - Madison, 1500 Engineering Dr., Madison, WI 53706, USA
E-mail contact of main author: dernst@psfc.mit.edu

Abstract: This work demonstrates local control of H-Mode density peaking with electron cyclotron heating and develops a quantitative understanding of the underlying mechanisms. Density gradient driven trapped electron modes are shown to dominate transport in the inner core of (quiescent) H-Mode plasmas with moderately peaked density profiles. The critical density gradient for onset of trapped electron mode (TEM) turbulence, the turbulence intensity, and transport are strongly sensitive to electron temperature. In DIII-D, we have demonstrated local control of H-mode density peaking with modulated electron cyclotron heating (ECH), and similarly in Alcator C-Mod with modulated minority ion cyclotron frequency heating. As particle and electron thermal transport increase in DIII-D QH-modes, newly observed coherent fluctuations in the inner core intensify near the heating location. Their wavenumbers are consistent with density gradient driven TEMs. Using a new synthetic diagnostic, nonlinear GYRO simulations closely reproduce the frequency spectrum of density fluctuations from Doppler backscattering when TEMs are dominant. Simultaneously, the GYRO simulations match the inferred particle and energy fluxes during intense core electron heating in DIII-D, and GS2 simulations match them in Alcator C-Mod. In addition, the critical density gradient for onset of TEM turbulent transport exhibits a nonlinear upshift, associated with zonal flow dominated states near threshold, as shown in GS2 simulations. This upshift increases strongly with collisionality and limits the density gradient in C-Mod H-mode experiments. In DIII-D, GYRO simulations show that ECH destabilizes density gradient driven TEMs by increasing T_e/T_i. As T_e approaches T_i and rotation is reduced, the density gradient driven TEM dominates transport in the inner core. In addition, shear in the parallel flow strongly drives the core instability prior to ECH. Toroidal rotation slows with ECH, reducing this drive. The results suggest a new mechanism for self-regulation of fusion power in self-heated plasmas.

1. Introduction

Density peaking in H-mode is frequently observed and would, if realized, impact fusion gain significantly. It is not clear whether H-mode density peaking will persist under reactor-relevant conditions. External electron heating appears to not only increase H-mode electron thermal transport, but also particle transport and momentum transport. The increased particle transport during certain forms of RF heating, particularly electron heating, is often characterized as "density pumpout," which may be partly a pedestal effect propagated to the core by profile stiffness. The controlled experiments presented here instead demonstrate a *local* core effect on particle transport associated with electron heating. We make use of steady edge localized mode (ELM)-free regimes on both Alcator C-Mod and DIII-D to study the transport and fluctuations in the inner core, where nearly all fusion power is produced. Nonlinear gyrokinetic simulations are used to develop a quantitative understanding of the mechanisms, shown to become increasingly important as the electron temperature approaches the ion temperature, and at low collisionality and torque.

The DIII-D experiments, conducted during the first National Fusion Science Campaign, demonstrate that H-mode core particle transport and density peaking can be locally controlled by modulated ECH. Even in H-modes with moderately peaked density profiles,

GS2 [1] and GYRO [2] simulations reveal that density gradient driven trapped electron modes (TEM) are the dominant drift modes in the inner half-radius, where the density profile responds to electron heating. Unlike temperature gradient driven TEMs, density gradient driven TEMs produce larger, ion scale fluctuations, similar to ion temperature gradient driven modes, and zonal flows play an important role [3].

New nonlinear gyrokinetic simulations using GS2 reveal that the effective critical density gradient, above which TEM turbulent transport becomes stiff, lies well above the linear threshold for instability at high collisionality. This non-linear upshift in the TEM critical density gradient $R/L_n^{crit} = -(R/a)\left[d\ln(n)/d\rho\right]\Big|_{crit}$ [4] is associated with zonal flow dominated states [5,6], and increases strongly with collisionality, as shown in Fig. 1, with zero temperature gradient. With realistic ion temperature gradients, the linear threshold increases (not shown), so that the nonlinear upshift exceeds the linear threshold by a smaller factor of 2–3. The C-Mod experiments are consistent with this prediction – the density gradient is effectively limited by the TEM non-linear critical density gradient during on-axis heating, which arrests density peaking as it increases with time. The DIII-D experiments explore the role of TEM turbulence at an order of magnitude lower collisionality (as indicated in Fig. 1).

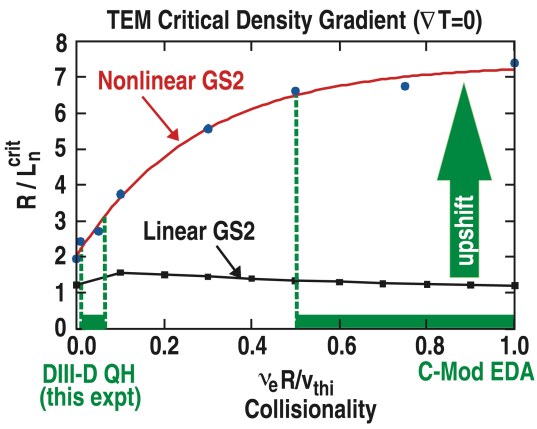

Fig. 1. Nonlinear upshift of TEM critical density gradient from 220 GS2 nonlinear simulations increases strongly with collisionality (Cyclone case, R/L_T=0).

2. Controlling H-mode Density Peaking in Alcator C-Mod with Electron Heating

In Alcator C-Mod, steady ELM-free H-mode plasmas (so called Enhanced D_α or EDA H-modes) heated with off-axis minority ion cyclotron resonance heating (ICRH) develop peaked density profiles following a relatively rapid transition to H-mode [7–10]. In the H-mode phase, the central density slowly rises over ~30 energy confinement times. Strong impurity accumulation leads to radiative collapse unless the density rise is arrested with on-axis minority ICRH [11]. The density can be maintained in steady state using on-axis ICRH where increasing the on-axis ICRH power flattens the density profile. The steep density gradient region in the EDA H-Mode inner core has historically been referred to as an internal transport barrier (ITB). Its formation exhibits a threshold in power and off-axis minority ICRH resonance location, but it does not rely on reversed magnetic shear or external torques, and does not exhibit rapid transitions characteristic of ITBs on other machines. We have previously shown that density gradient driven TEMs are dominant in the region shown in Fig. 2, and that nonlinear GS2 simulations match the inferred energy and particle fluxes [4,12] from TRANSP [13] analysis. The shape of the measured density fluctuation wavenumber spectrum from the 32 channel vertically line-integrated Phase Contrast

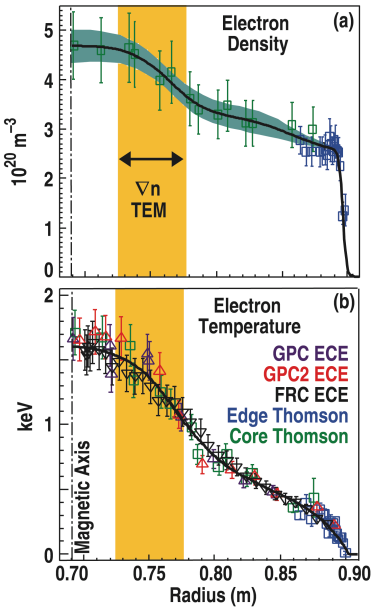

Fig. 2. Density and temperature profiles in Alcator C-Mod EDA H-mode plasma (T_i=T_e). The density gradient driven TEM is the sole instability in the steep density gradient "ITB" region (yellow band).

Imaging (PCI) system was closely reproduced using the GS2 nonlinear simulations with a synthetic diagnostic [5], during on-axis electron heating, when TEMs were dominant. We have revisited these experiments with significantly improved diagnostics [electron cyclotron emission (ECE) temperature profiles, improved Thomson scattering, absolutely calibrated PCI, HIREX Sr. argon x-ray spectroscopic measurements of ion temperature and rotation profiles, and a full suite of edge fluctuation measurements]. On-axis heating was modulated to separate the core and edge fluctuation response in the line-integrated PCI signal (Fig. 3). The density fluctuation intensity closely tracks the local on-axis electron temperature through individual sawteeth, while approximately doubling on average during the two during the on-axis heating pulses. At the same time, data from the magnetics (shown), the gas-puff imaging (not shown), and reflectometry (not shown) indicate strongly diminishing edge fluctuations during the on-axis heating pulses. This decrease in edge density and magnetic fluctuation levels contrasts with the increased density fluctuation level ñ from the PCI system, indicating that the PCI signal is dominated by the core fluctuations during on-axis heating. We have developed a new PCI synthetic diagnostic for GS2, mapping to an annulus in Cartesian coordinates (R,Z). Preliminary comparisons with absolutely calibrated PCI measurements match the PCI fluctuation level when the density gradient is increased to the top of its uncertainty range.

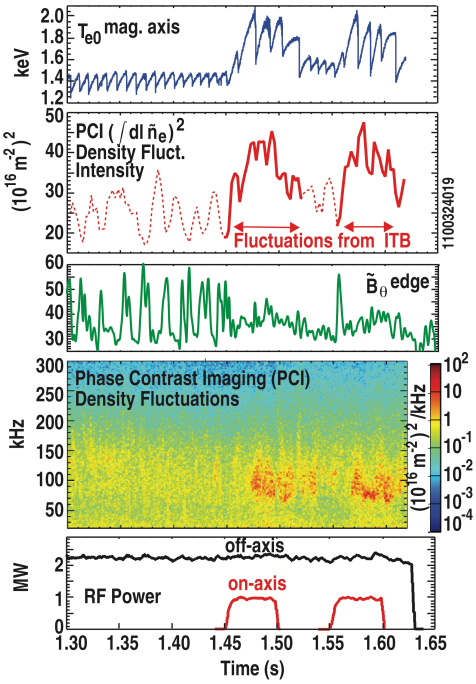

Fig. 3. Inner core density fluctuations intensify during on-axis minority ICRF electron heating of Alcator C-Mod ITB.

The strong increase in particle transport during on-axis heating is demonstrated in Fig. 4. The trajectory of the steep density gradient radius (r/a= 0.35) is shown as it evolves in time through a contour map of the maximum linear growth rate from GS2, as a function of density and temperature gradients. The density slowly peaks until being arrested by an on-axis heating pulse at 1.200 s. During on-axis heating, 1.200 to 1.227 s, the density gradient a/L_n is limited at a/L_n = 2.3–2.5, consistent with the nonlinear TEM critical density gradient in Fig. 1, well above the linear threshold (a/L_n=1.4). During heating, the collisionality is reduced, reducing the predicted nonlinear critical density gradient roughly 10%.

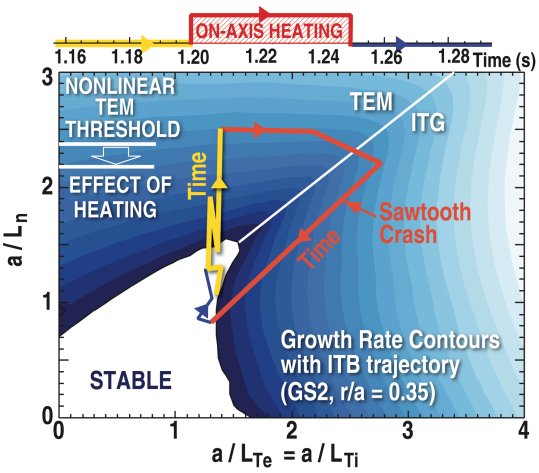

Fig. 4. Trajectory of the r/a=0.35 radius through a stability diagram created from 1200 GS2 simulations, spanning $k_\theta\rho_i$ = 0-4. The density peaking is arrested during on-axis heating, when the density gradient is limited by the effective nonlinear TEM critical density gradient.

Figure 5 shows a comparison of nonlinear GS2 simulations with TRANSP [13] transport analysis, during the on-axis heating at r/a=0.35, at the top of the trajectory shown in Fig. 4. The total heat flux from TRANSP is well-reproduced by the GS2 simulations [Fig. 5(a)]. Only the total heat flux is compared due to uncertainty in the ion-electron energy exchange when $T_i \approx T_e$.

The GS2 simulations are shown as a function of density gradient, which is both the

main driving factor for the most-unstable mode (TEM), and the main source of uncertainty [indicated by the horizontal error bar in Fig. 5(c)]. Figure 5(b) shows that the transport by density gradient driven TEM turbulence dominates for $a/L_n>2.2$, with the electron channel flux q_e accounting for most of the heat flux q_e+q_i. Finally, Fig. 5(c) shows that the GS2 particle flux is minimized between the ion temperature gradient (ITG) and TEM dominated regimes, and balances the Ware pinch within uncertainty. However, at the nominal density gradient at which the energy flux matches experiment, the GS2 particle flux exceeds the Ware pinch to produce a finite net flux in the absence of sources, suggesting the GS2 simulation may overestimate the particle flux.

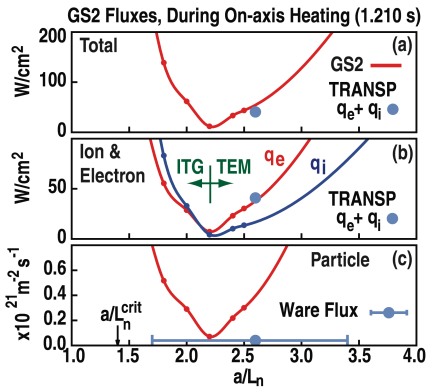

Fig. 5. (a) GS2 nonlinear TEM simulations at r/a=0.35 match the TRANSP energy flux at the nominal ITB density gradient, (b) the TEM energy flux is dominated by the electron channel, and (c) the particle flux balances the Ware flux for a/L_n~2.2, within uncertainty.

3. Controlling QH-mode Density Peaking in DIII-D with Electron Heating

Dedicated experiments utilizing the quiescent H-mode regime [14–16] allow us to study the effect of ECH on inner core transport under controlled conditions, without ELMs or sawteeth ($q_{min}>1.4$). Density profiles are measured by reflectometry, with full profile coverage for $\rho>0.1$, while density fluctuations are measured locally by Doppler backscattering (DBS) [17], with selectable radius and wavenumber.

To avoid large fast ion densities, which make comparison with gyrokinetic simulations more difficult [18,19], we transition from counter-current dominated neutral beam torque to a near-balanced torque phase to raise the density. The central density was then reduced, by adding counter torque, to 5.5×10^{19} m^{-3} for improved mm-wave diagnostic coverage and to avoid ELMs during ECH. The fast ion density in these cases from ONETWO [20]/ NUBEAM [21] and TRANSP [13] is <12% of the electron density. After transitioning to the low counter-current torque phase at 2.5 s, conditions were held steady from 3.0 to 5.0 s, during which ECH was applied, maintaining the beam power at 5.5 MW. Pro-files with and without ECH are shown in Fig. 6, at 2.98 s immediately prior to the first 3.4 MW ECH pulse, and at 3.08 s, near the end of the first ECH pulse. The effect of ECH, injected at $\rho=0.22$, is to raise the electron temperature by 50%, locally flatten the density profile for $\rho<0.4$, slow the toroi-dal rotation over the whole profile includ-ing the pedestal, and

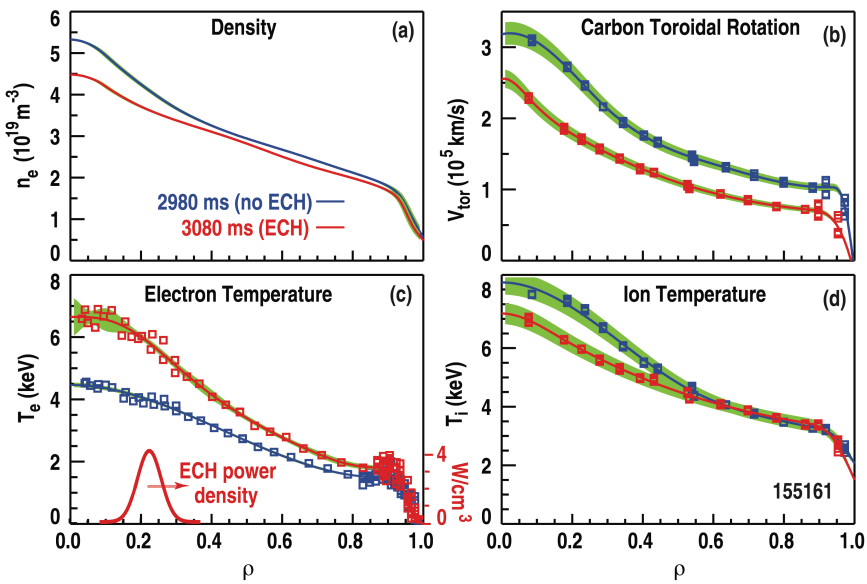

Fig. 6. Adding 3.6 MW ECH at $\rho=0.22$ (red) locally controls density peaking in the inner core by increasing T_e and T_e/T_i. (a) Reflectometer density profiles, (b) charge exchange recombination (CER) toroidal velocity profiles, (c) ECE and Thomson scattering electron temperature, and (d) CER ion temperature. Uncertainty ranges shown in green.

modestly reduce the ion temperature. The QH-mode pedestal is regulated by edge harmonic oscillations (EHO), driven in part by rotation. The EHO drive is reduced during ECH, so that the ECH duration is limited by ELM onset.

Focusing on the particle transport, Fig. 7 shows the evolution of the density at fixed radial locations across the plasma. The density responds to modulated ECH locally in the inner half-radius, while responding weakly in the outer half-radius. The density gradient driven TEM is dominant in this region during ECH, and would be expected to drive strong particle (and impurity) transport. The driving factor for TEM, a/L_n, decreases during ECH pulses, as would be expected if the TEM transport increases during ECH [Fig. 7(b)].

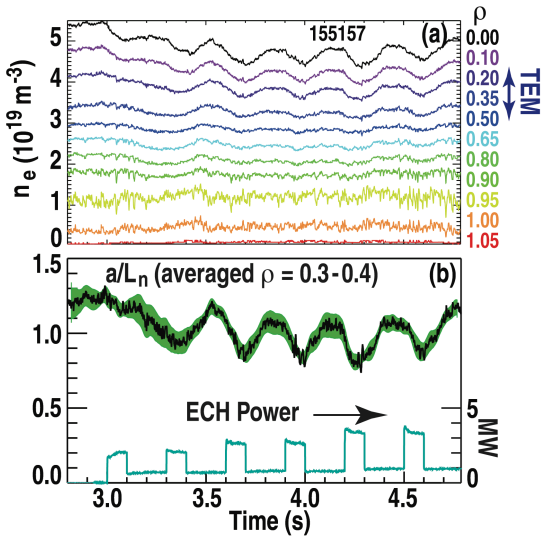

Fig. 7. (a) Density measured by the profile reflectometer with 2-4 mm radial resolution, at 0.4 ms intervals, responds to modulated ECH only in the inner core, where the density gradient driven TEM dominates. (b) The TEM driving factor a/L_n is modulated by ECH.

The mechanism leading to the increased particle transport with ECH is the following: ECH increases T_e by 50%, leading to $T_e \approx T_i$ in the inner core, which reduces the TEM linear critical density gradient by half This is shown in Fig. 8(a), which compares the inverse density gradient scale length $a/L_n = -(1/n)dn/d\rho$, from the profile reflectometer, with the critical gradient a/L_n^{crit} from GYRO eigensolver calculations (shown without parallel flow). This significantly increases the net effective TEM growth rate $\gamma_{net} = \gamma - \alpha_E\gamma_E$ [Fig. 8(b)] in the inner core, where γ is the TEM growth rate including parallel flow. Here the parallel flow is given by $Ma=\Omega_0R_0/c_s$ and its shear, γ_P, where $\Omega_0(\rho)\approx E_r/RB_p$ is approximately the toroidal angular velocity, $\gamma_E = r/q\ d/dr(E_r/RB_p)$ is the ExB shear rate, and $\gamma_P=qR_0/r\ \gamma_E$. The growth rates are plotted at $k_y\rho_s= 0.5$ (the wavenumber selected by DBS), using the shear factor $\alpha_E=0.68$, discussed below. Importantly, using the GYRO eigenmode solver shows the destabilizing effect of parallel flow shear in the no ECH case overcomes the stabilizing effect of finite Mach number, to more than double the growth rate over the entire TEM range of wavenumbers. Without sheared parallel flow, the inner core would be stabilized entirely by ExB shear and exhibit no transport without ECH. During ECH, the effect of sheared parallel flow drive is seen only at shorter wavelengths. The nonlinear GYRO simulations of TEM turbulence in the ECH case show that the effect of ExB shear on the energy and particle fluxes closely matches a scaling [22] for the linear quench rule, $\alpha_E(\kappa,\varepsilon) = 0.71(\kappa/1.5)(R_0/3a)^{0.60} = 0.68$ from simulations of ITG turbulence, which reduces fluxes by the factor 0.4.

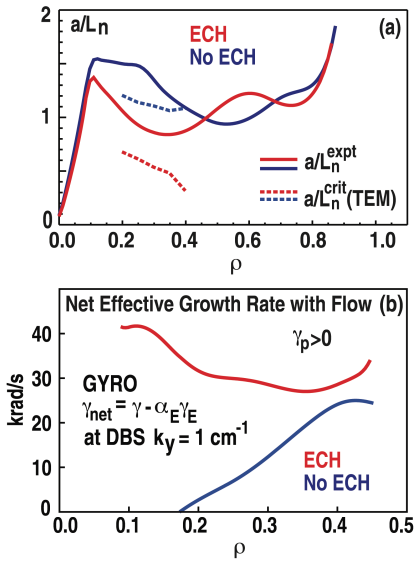

Fig. 8. (a) Measured density gradient a/L_n compared with TEM linear critical density gradient a/L_n^{crit} from GYRO. (b) Net effective growth rate for ECH and no ECH case including ExB shear and parallel flow shear. The net growth rate is much higher with ECH.

Detailed transport and profile analysis was carried out using three iterations of ONETWO, NUBEAM, and kinetic EFIT [23] constrained by E_r-corrected MSE q-profiles, and with TRANSP. Charge exchange spectroscopy data for carbon was analyzed with

CERFIT and corrected for the cross-section energy dependence. Electron temperature profiles from ECE were used in the core, with Thomson scattering for the pedestal. Density profiles were calculated directly from profile reflectometer phase data, without fitting, smoothing, or other processing for ρ>0.1, preserving their 2–4 mm radial accuracy and 10% uncertainty in a/L_n. Comparing the two times 2.98 s and 3.08 s for shot 155161, at ρ=0.30, the TRANSP and ONETWO analysis shows that the addition of 3.4 MW of ECH centered at ρ=0.22 increases the electron heat flux by an order of magnitude to 3.3 MW, doubles the ion heat flux to 0.8 MW, and does not change the particle flux. Consistent with the factor of 2 reduction in density gradient, TRANSP shows the effective total particle diffusivity doubles with ECH. GYRO nonlinear simulations of the same ECH case (155161 at 3.08 s, ρ=0.30), including finite toroidal Mach number and sheared parallel flow, are in close agreement with the particle and thermal fluxes inferred from transport analysis, as shown in Fig. 9. The increase of the fluxes with the TEM driving factor a/L_n, above the linear threshold a/L_n^{crit}, is consistent with dominant density gradient driven TEM turbulent transport. Similar to the GS2 results for Alcator C-Mod, GYRO matches the particle flux for a lower value of than a/L_n than for the heat fluxes. Zonal flows are dominant over the TEMs for $a/L_n < 0.6$, which, together with the break in slope of the flux curves, suggests an effective nonlinear TEM critical density gradient $a/L_n^{crit} \approx 0.65$, ~36% above the linear threshold, following the qualitative trend in Fig. 1.

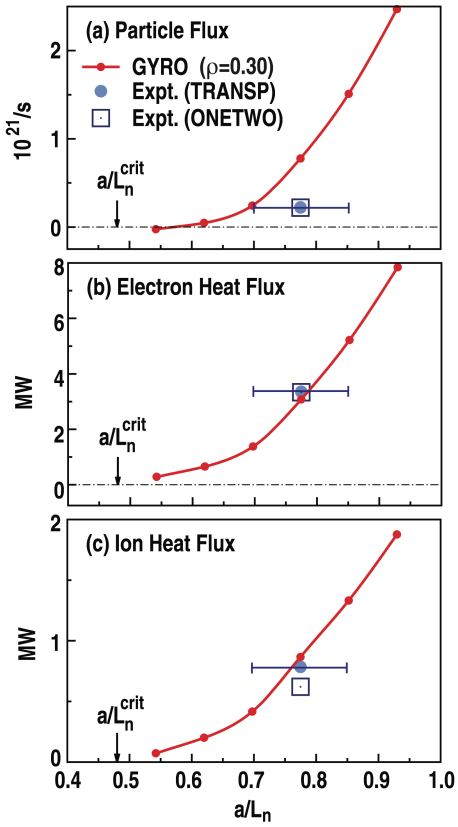

Fig. 9. Nonlinear GYRO gyrokinetic simulations during ECH, for shot 155161 at ρ=0.30. (a) Particle flux, (b) electron heat flux, (c) ion heat flux.

4. New Coherent Modes at TEM Wavelengths and Fluctuation Spectrum Comparison with GYRO/Synthetic DBS

Doppler backscattering measurements for these experiments have revealed new coherent density fluctuations (or discrete "modes") accompanied by broadband turbulence, as shown in Fig. 10 (155161, ρ=0.28). Positive frequencies correspond to the electron diamagnetic direction in the laboratory frame. The new coherent modes have wavenumbers $k_y\rho_s \approx 0.5$ in the TEM range. These density fluctuations intensify during ECH, together with the broadband turbulence, shown in Fig. 11(a).

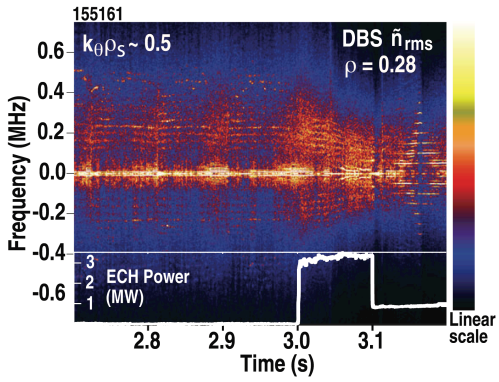

Fig. 10. Frequency spectrum of inner core density fluctuations from DBS reveals high frequency quasi-coherent modes prior to ECH, with stronger broadband turbulence at TEM wave-numbers during ECH. Toroidal rotation slows during ECH, reducing Doppler broadening.

Low frequency EHO harmonics are also observed at frequencies up to 70 kHz on DBS, magnetics, and the CO_2 laser interferometer, but their frequencies do not follow the core toroidal rotation, and their interval is much smaller than the 30 kHz interval seen at higher frequencies. Slightly farther out in radius, near ρ=0.43, a strong increase in spectral power is seen at shorter wavelengths, $k_y\rho_s \approx 3.5$ [Fig. 11(b)], also in the electron

diamagnetic direction in the lab frame. ETG modes become increasingly unstable beyond ρ>0.35 during ECH in GYRO simulations (not shown).

The DBS measurements are most sensitive to a binormal (~polodial) wavenumber $k_y \approx 1\ cm^{-1}$, with a negligible radial component. Full-wave simulations in 2D [24] suggest a Gaussian response function for power spectral density, with estimated half-width $\Delta k \approx 0.94\ cm^{-1}$. DBS is therefore sensitive to a band of toroidal mode numbers n determined by $k_y = nq(\rho,\theta)/r_{cyl}(\rho,\theta)$, where $q(\rho,\theta)$ is the "local" poloidally varying safety factor with average value $q(\rho)$, and $r_{cyl}(\rho,\theta)$ is the local cylindrical minor radius at the DBS cutoff location, with response $R(n) = \exp[-(n-n_0)^2/(\Delta n)^2]$, where $n_0 \approx 19$ and $\Delta n \approx 18$ at 298 s.

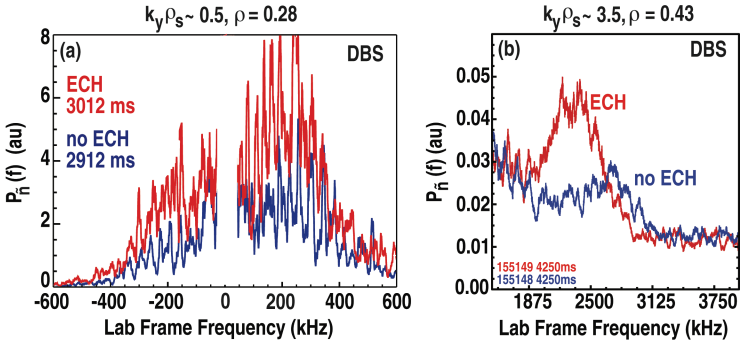

Fig. 11. (a) Density fluctuation power spectral density from DBS, near the radius and wavenumber of maximum TEM growth rate. (b) DBS density fluctuations at $k_y\rho_s$~3.5 also increase in intensity during ECH farther out in radius (ρ=0.43), where ETG modes are found to be unstable.

Prior to ECH at 3.0 s, the frequencies of the coherent modes are separated by a nearly constant interval 30 kHz in the lab frame. In this case, CER measurements indicate that $E_r \approx V^C_{tor} B_p$, where V^C_{tor} is the carbon toroidal velocity and B_p is the poloidal magnetic field, so that the Doppler shift is given by $k_y v_E \approx n\Omega_0$, where $\Omega_0 = V^C_{tor}/R$. The frequencies from GYRO are small relative to the Doppler shift, on with adjacent toroidal mode numbers separated by 0.6 kHz. If the coherent modes have adjacent toroidal mode numbers, their lab frame frequency interval would be $\Omega_0/2\pi$=14–20 kHz from the CER Doppler shift alone.

Here we present the first direct comparison of the frequency spectrum from nonlinear GYRO simulations with DBS in DIII-D. We have developed a new GYRO synthetic diagnostic for DBS that accurately accounts for flux surface shaping, and extends previous work [25] to allow detailed comparison with measured frequency spectra, with results shown in Fig. 12. The DBS data shown in Fig. 12(a) were taken from Fig. 10 at the time shown and binned in frequency to compare directly with the initial GYRO results, which are also binned in frequency. The frequency spectrum from nonlinear GYRO simulations, during ECH (155161, ρ=0.30, 3080 ms), closely reproduces the shape of the DBS frequency spectrum. Note that initial GYRO simulations for the no ECH case (with strong shear in parallel flow) present numerical challenges that are currently being resolved, and are not shown. Because DBS is not absolutely calibrated, we have normalized it to match the spectral peak from GYRO. The shape of the DBS frequency spectrum prior to ECH, at 2.98 s is much broader and attains roughly half the power spectral density as the ECH case. This trend is reproduced by the net GYRO linear growth rate (details discussed above) including parallel flow. In Fig. 12(b), the net growth rate has been weighted by the DBS wavenumber response. Nonlinearly the GYRO spectrum peaks at $k_y\rho_s$=0.3 at 3.08 s (corresponding to a Doppler shifted frequency 153 kHz), which is downshifted from the wavenumber of maximum linear growth rate, $k_y\rho_s$=0.85. Finally, GYRO matches the shape of the DBS spectrum over four orders of magnitude on a log scale (not shown). However, as remarked above, the simulated frequency spectrum, which relies on the Doppler shift computed from the CER measured toroidal rotation, appears to be downshifted in frequency relative to the DBS spectrum. Taking the Doppler shift from the frequency interval between the coherent modes would shift the GYRO spectrum upward in frequency by ~75 kHz to more closely reproduce the measured DBS spectrum.

5. Summary

Density gradient driven trapped electron modes are found to dominate inner core transport in moderately peaked H-mode plasmas in both C-Mod and DIII-D, allowing local control of density peaking with electron heating. Gyrokinetic simulations reproduce the particle, electron thermal, and ion thermal energy fluxes in the experiments within measurement uncertainty. New coherent core density fluctuations in DIII-D intensify during ECH and appear consistent with density gradient driven trapped electron modes. Nonlinear gyro-kinetic simulations, using a synthetic DBS diagnostic in DIII-D, closely reproduce the measured frequency spectrum of broadband density fluctuations with ECH. A new nonlinear upshift in the TEM critical density gradient is confirmed. This work illustrates a potential mechanism for the self-regulation of fusion power in self-heated fusion plasmas, and improves quantitative predictions of transport in the inner core under the relevant conditions.

This material is based upon work supported in part by the US Department of Energy, Office of Science, Office of Fusion Energy Sciences, using the DIII-D National Fusion Facility, a DOE Office of Science user facility, under Awards DE-FC02-08ER54966, DE-FC02-04ER54698, DE-AC02-09CH11466, DE-FG02-08ER54984, DE-FG02-07ER54917, DE-FG02-99ER54531, DE-FG02-89ER53296, DE-FG02-08ER54999, DE-FC02-99ER54512, DE-AC02-5CH11231 (NERSC). We gratefully acknowledge J. Candy (General Atomics) for developing the GYRO code. DRE, WG and AMD acknowledge an Advanced Leadership Computing Challenge Award at NERSC from the Office of Advanced Scientific Computing Research.

References

[1] DORLAND, W. *et al.*, Phys. Rev. Lett. **85** (2000) 5579.
[2] CANDY, J. and WALTZ, R.E., J. Comput. Phys. **186** (2003) 545.
[3] ERNST, D.R. *et al.,* Phys. Plasmas **16** (2009) 055906.
[4] ERNST, D.R. *et al.*, Phys. Plasmas **11** (2004) 2637.
[5] ERNST, D.R. *et al.*, in *Proc. 21st IAEA Fusion Energy Conf., Chengdu, China*, paper IAEA-CN-149/TH/1-3 (2006).
[6] ERNST, D.R. "Nonlinear Upshift of Trapped Electron Mode Critical Density Gradient: Simulation and Experiment," Invited talk, *54th APS/DPP Meeting, Providence, Rhode Island* (2012).
[7] RICE, J.E. *et al.*, Nucl. Fusion **41** (2001) 277.
[8] FIORE, C.L. *et al.*, Plasma Phys. Control. Fusion **46** (2004).
[9] FIORE, C.L. *et al.*, Phys. Plasmas **11** (2004) 2480.
[10] ZHUROVICH, K. *et al.,* Nucl. Fusion **47** (2007) 1220.
[11] WUKITCH, S.J. *et al.*, Phys. Plasmas **9** (2002).
[12] ERNST, D.R. *et al.*, in *Proc. 20th IAEA Fusion Energy Conf., Vilamoura, Portugal*, IAEA-CN-116/TH/4-1 (2004).
[13] HAWRYLUK, R.J. *An Empirical Approach to Tokamak Transport", in Physics of Plasmas Close to Thermonuclear Conditions*, ed. by B. Coppi, et al., (CEC, Brussels, 1980) Vol. 1, p. 19.
[14] BURRELL, K.H. *et al.*, Phys. Plasmas **82,** 153 (2001).
[15] DOYLE, E.J. *et al.*, Plasma Phys. Control. Fusion **43** (2001) A95.
[16] GREENFIELD, C.M. *et al.,* Phys. Rev. Lett. **20** (2001) 4544.
[17] RHODES, T.L. *et al.*, Rev. Sci. Instrum. **81** (2010) 10D912.
[18] HOLLAND, C. *et al.*, Nucl. Fusion **52** (2012) 114007.
[19] SCHMITZ, L. *et al.*, Nucl. Fusion **52** (2012) 023003.
[20] PFEIFFER, W.W. *et al.*, "ONETWO: A Computer Code for Modeling Plasma Transport in Tokamaks," General Atomics Report GA-A16178 (1980).
[21] GOLDSTON, R.J. *et al.*, J. Comp. Phys. **43** (1981) 61.
[22] KINSEY, J.E. *et al.*, Phys. Plasmas **14** (2007) 102306.
[23] LAO, L.L. *et al.,* Nucl. Fusion **30** (1990) 1035.
[24] HILLESHEIM, J. C. *et al.*, Rev. Sci. Instrum. **83** (2012) 10E331.
[25] HOLLAND, C. *et al.,* Nucl. Fusion **52** (2012) 063028.

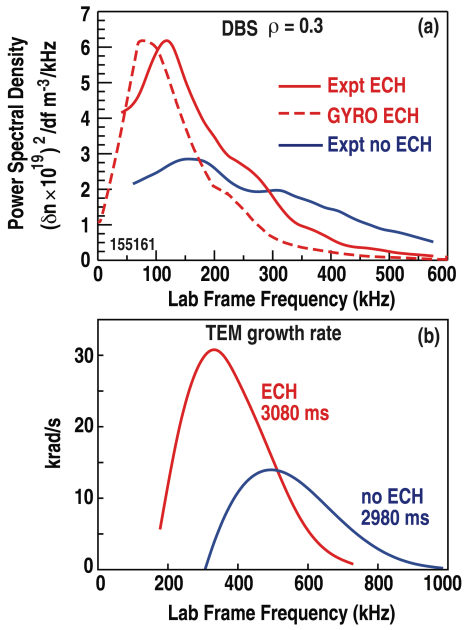

Fig. 12. (a) GYRO nonlinear simulations with synthetic diagnostic reproduce DBS spectrum during ECH, (b) GYRO linear growth rates, weighted by the DBS response, qualitatively reproduce changes with ECH.